Vol. 13 • No. 9 • April 5 • 2024

www.advhealthmat.de

ADVANCED HEALTHCARE MATERIALS

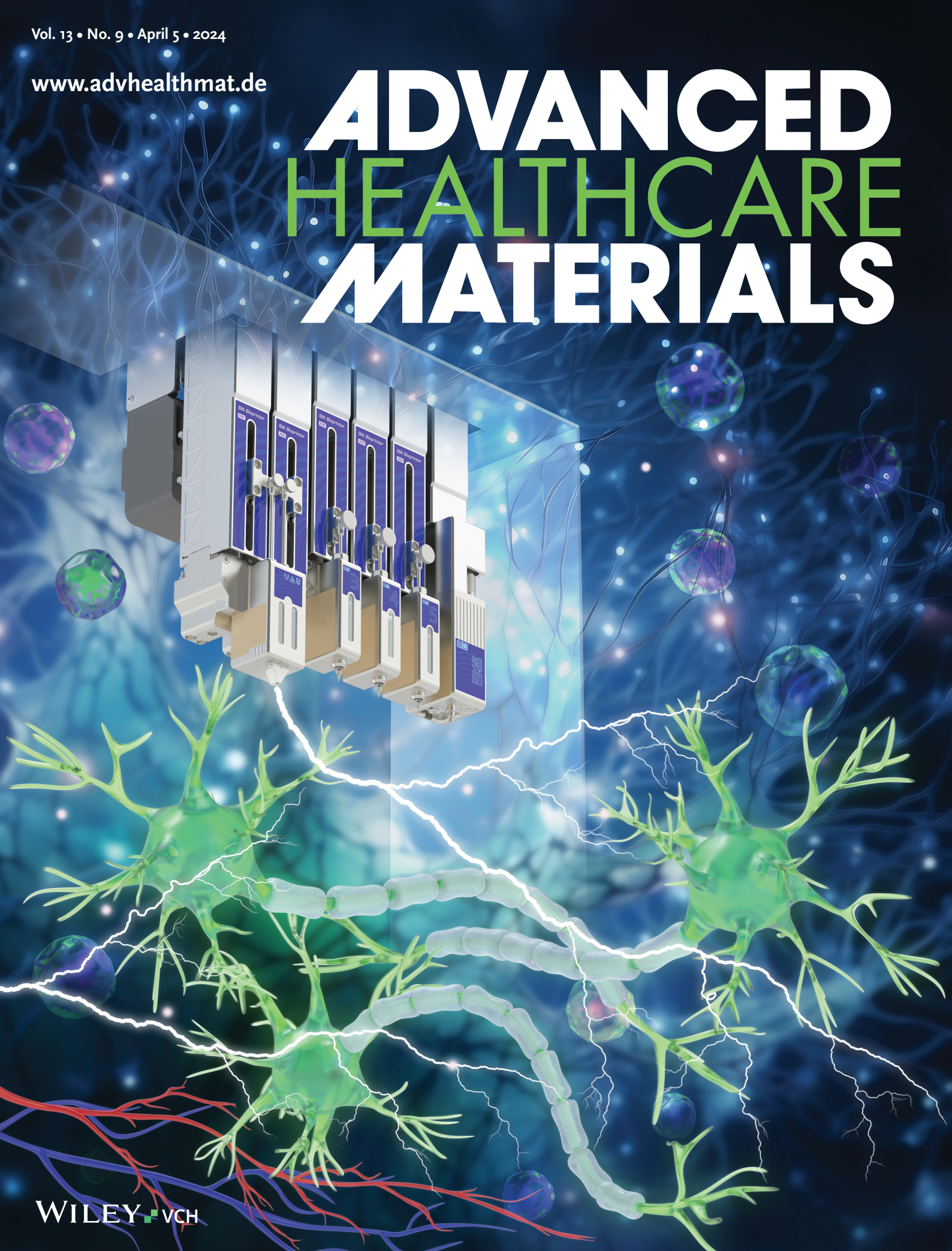

WILEY VCH

ADVANCED HEALTHCARE MATERIALS
www.advhealthmat.de

Quantitative Biofabrication Platform for Collagen-Based Peripheral Nerve Grafts with Structural and Chemical Guidance

Heran Wang, Yiming Hao, Kai Guo, Lianqing Liu, Bing Xia, Xue Gao, Xiongfei Zheng, and Jinghui Huang**

Owing to its crucial role in the human body, collagen has immense potential as a material for the biofabrication of tissues and organs. However, highly refined fabrication using collagen remains difficult, primarily because of its notably soft properties. A quantitative biofabrication platform to construct collagen-based peripheral nerve grafts, incorporating bionic structural and chemical guidance cues, is introduced. A viscoelastic model for collagen, which facilitates simulating material relaxation and fabricating collagen-based neural grafts, achieving a maximum channel density similar to that of the native nerve structure of longitudinal microchannel arrays, is established. For axonal regeneration over considerable distances, a gradient printing control model and quantitative method are developed to realize the high-precision gradient distribution of nerve growth factor required to obtain nerve grafts through one-step bioprinting. Experiments verify that the bioprinted graft effectively guides linear axonal growth in vitro and in vivo. This study should advance biofabrication methods for a variety of human tissue-engineering applications requiring tailored cues.

1. Introduction

Artificial tissues and organs offer a promising permanent solution to their damaged biological counterparts.[1] In recent decades, 3D bioprinting technology has received considerable attention owing to its potential for the fabrication of biomaterials in tissue and organ bioengineering, such as the liver,[2] heart,[3] and bones.[4] Synthetic polymers are predominantly utilized as biomaterials in 3D bioprinting due to their facile processability. This characteristic allows these materials to be readily molded and tailored to accommodate specific requirements. However, the extracellular matrix (ECM) performs a crucial role in the formation and regeneration of tissues and organs. The ECM not only provides dynamic 3D structural support for cells and tissues, but also orchestrates cell signaling, functions, properties, and morphology,[5] making it attractive for the biofabrication of artificial tissues and organs. However, owing to their high molecular weight and higher-order structure, the main components of ECM have limited solubility and high viscoelasticity,[6] making them difficult to manipulate during 3D bioprinting because they collapse easily.

Collagen is the most abundant component of the ECM and exists widely in vertebrates.[7] Collagen, together with other ECM components, provides a structural framework for tissue development and function, and triggers various cellular signaling pathways via its interaction with cell receptors.[7] Therefore, collagen is an ideal material for tissue regeneration and has long been the focus of tissue biofabrication.[8] However, because collagen is soft and tends to sag during printing, it is difficult to directly print 3D complex tissue grafts with high fidelity. Feinberg et al. recently proposed a method for printing collagen into a heart-like model that enables rapid cellular infiltration and microvascularization, shedding light on the construction of complex tissue or organ structures using collagen in biofabrication.[3] Nonetheless, different tissues exhibit unique structural and biological functions that have distinctive requirements for bioprinting. For example, the peripheral nerve has a unique longitudinal microchannel array structure, which guides axonal growth from the spinal cord to the terminal target muscles. Therefore, the longitudinal microchannel array is an essential structural cue for directing axonal growth. Additionally, during nerve regeneration, damaged axons must be regenerated over long distances to restore neuronal functions. However, it has been recognized that

H. Wang, K. Guo, L. Liu, X. Zheng
State Key Laboratory of Robotics
Shenyang Institute of Automation
Chinese Academy of Sciences
Shenyang 110016, China
E-mail: zhengxiongfei@sia.cn
H. Wang, K. Guo, L. Liu, X. Zheng
Institutes for Robotics and Intelligent Manufacturing
Chinese Academy of Sciences
Shenyang 110169, China
H. Wang
University of Chinese Academy of Sciences
Beijing 100049, China
Y. Hao, B. Xia, X. Gao, J. Huang
Department of Orthopaedics
Xijing Hospital
The Fourth Military Medical University
Xi'an 710032, China
E-mail: huangjh@fmmu.edu.cn
The ORCID identification number(s) for the author(s) of this article can be found under https://doi.org/10.1002/adhm.202303505

DOI: 10.1002/adhm.202303505

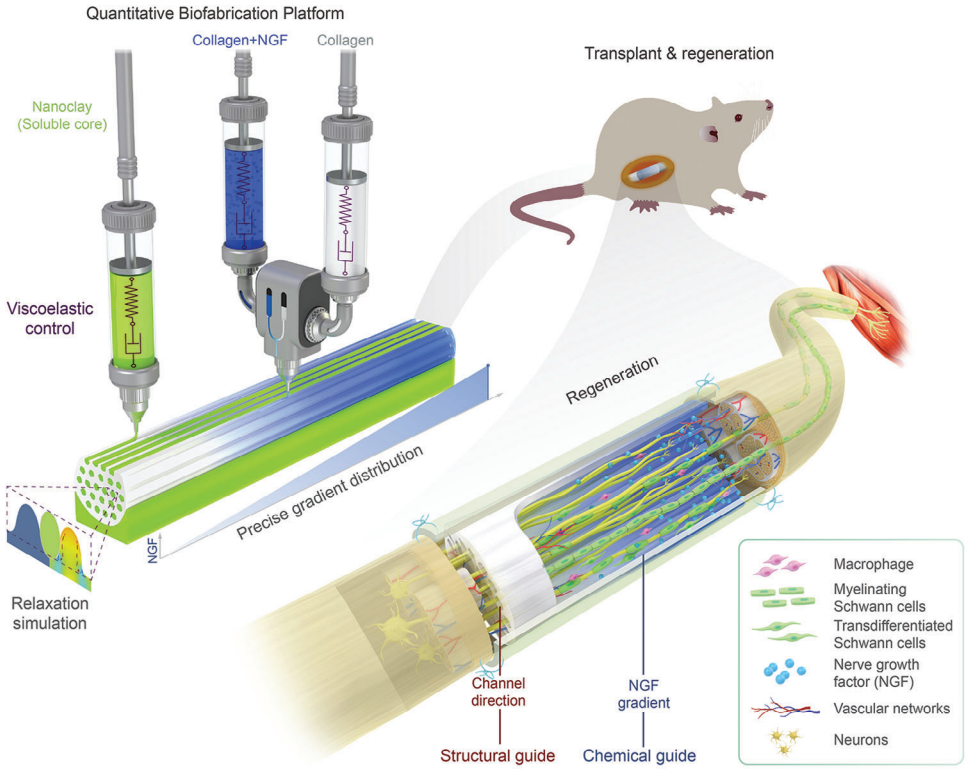

Figure 1. Schematic diagram of quantitative biomanufacturing process for collagen peripheral nerve grafts that can be transplanted into rats for nerve guidance repair. By identifying the viscoelastic properties of collagen and nanoclay ink, and simulating the stacking and relaxation process, we construct precise high-density microchannel arrays to achieve structural guidance for neural regeneration. Through a controlled viscosity and elasticity algorithm, we distribute a precise gradient of growth factors, providing chemical guidance for nerve regeneration.

the structural cues[9–11] alone are insufficient to sustain axonal regeneration across a long distance (>30 mm in humans). It is preferable to encourage axonal regeneration by combining native structures with chemical guidance,[12] such as the gradient distribution of neurotrophic factors from the proximal to distal nerve stumps.[13] Nonetheless, printing collagen into a neural graft with an intrinsic longitudinal microchannel array structure results in structural distortion during multi-material assembly due to the viscoelastic creep behavior of collagen. In addition, achieving real-time control over the precise neurotrophic factor ratio poses a significant challenge, given the lack of a precise microextrusion control method for viscoelastic inks. Consequently, the integration of chemical cues into collagen-based nerve-like structures using a one-step bioprinting approach[14–18] remains a challenge.[19]

In this study, we develop an integrated quantitative biofabrication platform for the fabrication of collagen nerve grafts. The platform enables us to i) use unmodified collagen as a bio-ink for high-precision multi-material bioprinting; ii) create a nerve structure of longitudinal microchannel arrays to guide axonal growth; iii) integrate nerve growth factor (NGF) gradients into the bioprinted nerve graft to facilitate neural chemotaxis for long-distance nerve regeneration; iv) improve the mechanical properties by using a high collagen concentration of 50 mg mL^{-1}. Within the constraints of a rigorously regulated rat model, a bioprinted nerve graft was empirically validated to effectively facilitate nerve regeneration over a distance of 12 mm (**Figure 1**). Given that the precise fabrication of delicate structures and the gradient distribution are common requirements for constructing 3D tissues, we believe that our platform, which was initially designed for collagen nerve grafts, has broad applicability in the field of regenerative medicine.

2. Results

2.1. High-Precision Bioprinting of Collagen Microchannel Array Structure

Collagen is the predominant component of the ECM in human tissues and provides remarkable biofunctionality. However, fabricating refined biomimetic microstructures from collagen is challenging owing to its soft properties.[20] To address this issue, we developed a multi-material bioprinting approach to create a collagen nerve graft with high-density microchannels. In this method, a sacrificial core material is employed to occupy the channel voids, which is subsequently dissolved after acidic collagen fixation. The primary obstacle to this process is the uncontrolled creep of extruded collagen filaments over time, which can result in misaligned and blocked channels. Therefore, it is imperative to establish a mechanical analysis model for collagen to calculate its transient deformation and guide the regulation of printing parameters.

Initially, we devised a Burgers model identification method to establish a robust analytical model for collagen. The Burgers

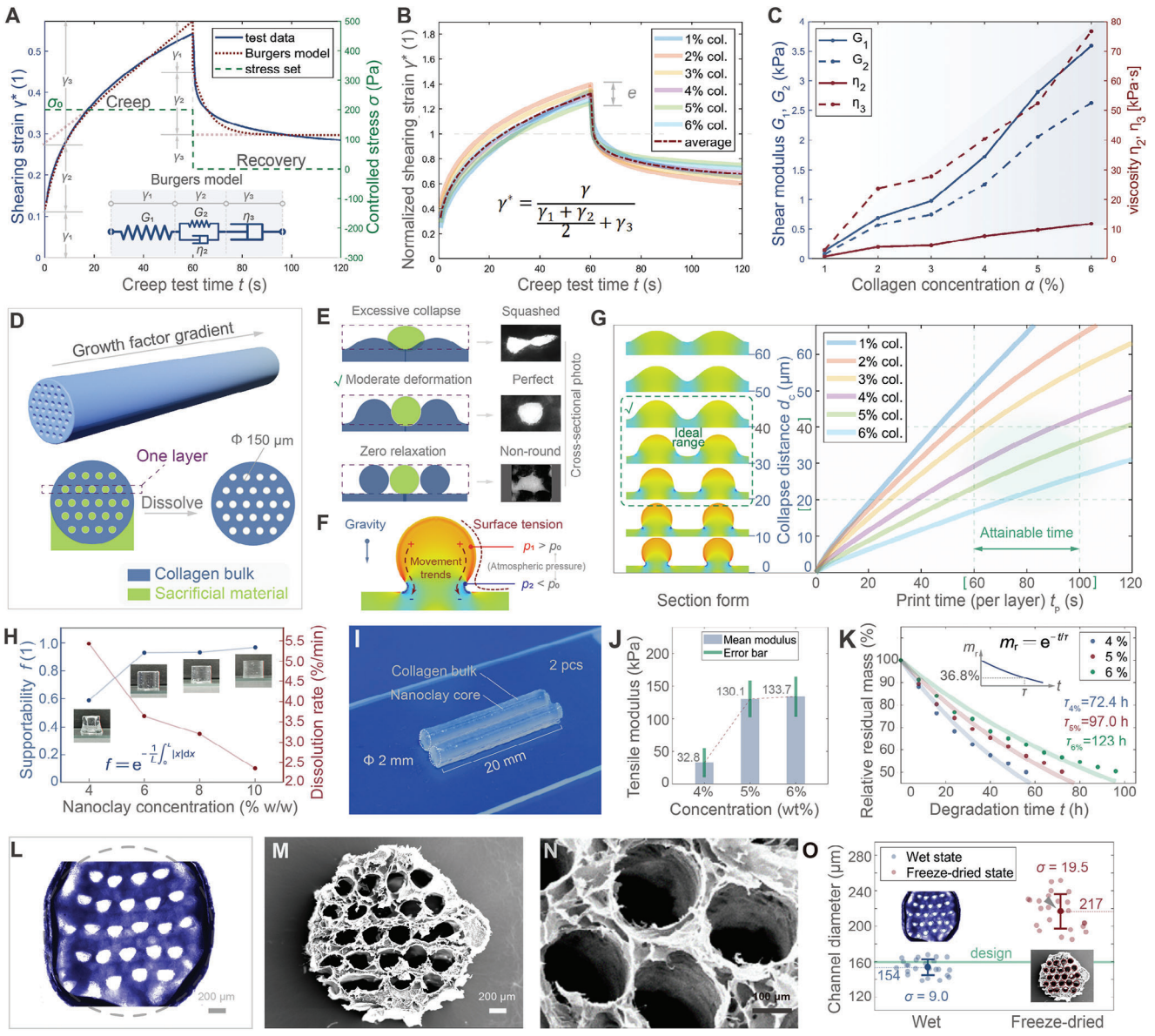

Figure 2. Quantitative analysis and manufacturing method for collagen microchannel array structure. A) Identification of collagen Burgers model parameters based on creep-recovery test. B) Consistency characterization of the collagen regularization model with different concentrations. C) Trend of Burgers model discrimination parameters by collagen concentration. D) Schematic of collagen nerve graft structure. E) Three assembly effects of the adhesive and soluble core materials due to the different mechanical behavior of the adhesive material with different concentrations. F) Simulation of kinetic behavior of collagen filament cross-sectional infiltration based on Burgers model parameters. G) Deformation of different collagen concentrations over time, including surface shape and collapse amount. H) Supportability and dissolution rate of nanoclay with different concentrations of soluble core material. I) Photograph of microchannel array of collagen neural graft print. J) Tensile modulus testing of collagen grafts with different concentrations. K) Degradation tests of collagen grafts with different concentrations. The degradation process can be characterized by an exponential decay function. L) Cross-sectional photograph of the wet state neural graft after removal of the soluble core under optical microscope. M) Overall electron micrograph after freeze-drying treatment. N) Local electron microscope photograph after freeze-drying. O) Statistical results on the diameter of nerve grafts in wet and freeze-dried states.

model, a four-variable theoretical framework, effectively captures the viscoelastic properties of materials by elucidating their response to external forces through deformation and stress-relaxation processes.[21] A rotational rheometer was employed to apply a stress curve (green dashed line) as an external force to obtain the strain curve of the creep recovery process (**Figure 2A**). By using the least-squares algorithm, we identified the four parameters of the Burgers model (G_1, G_2, η_2, and η_3) for various collagen concentrations (Figure S1, Supporting Information). For the collagen hydrogel, we determined that the Burgers model fit well with fewer parameters than other models, such as the Maxwell, Kelvin–Voigt, and elastic–viscoelastic–plastic models.[21] We plotted the normalized creep-recovery curves for collagen concentrations from 1% to 6% w/w (at 1% intervals)

in Figure 2B, which showed consistent behavior within the specified concentration range. Additionally, we generated a plot (Figure 2C) showcasing the relationship between the collagen concentration and the four model parameters we identified. Notably, this plot exhibited a promising linear trend, which is a crucial requirement for facilitating finite element analysis.

In order to mimic the intricate structure of the connective tissue sheaths present in peripheral nerves, we developed a collagen graft with a diameter of 2 mm. This graft was specifically designed to contain 24 channels, resulting in a high channel density of up to 7.6 channels per square millimeter (Figure 2D). These connective tissue sheaths are vital components of peripheral nerves, providing essential support and protection.[22] To achieve the desired high-density channel structure, we used a single soluble core filament with a diameter of 160 μm to form individual channel. In preliminary experiments, we observed a direct correlation between the mechanical properties of collagen and the channel morphology, which could be classified into three distinct categories (Figure 2E): including excessive collapse, moderate deformation, and zero relaxation. Excessive collapse of the collagen graft occurs when a low concentration of collagen is used, resulting in material misalignment and flattening of the soluble core. This leads to channel blockage and crosstalk between adjacent microchannels. Zero relaxation, another extreme case, occurs when using either an excessively high concentration of collagen, which results in excessively long relaxation times, or when printing in a liquid bath with excessively low interfacial tension. In these cases, we observed rough and irregular channel walls, poor adhesion between collagen fibers, and fragile graft structures. To quantitatively analyze the relaxation behavior of collagen, we developed a finite element model that incorporated Burgers viscoelasticity, surface tension, and gravity (Figure 2F). To simulate the dynamic behavior of collagen, we input the parameters of the analytical collagen model at various concentrations into the finite element model, which enabled us to capture the collapse and cross-sectional deformation over a period of 120 s (Figure 2G). Our computational analysis of collagen morphology indicated that the displacement range for moderate collapse was 20–40 μm. By combining this information with the attainable printing time interval of 60–100 s (due to printing speed limitations), we identified a suitable collagen concentration range between 4% and 6% w/w. This computational model can be used as a guide for selecting the appropriate collagen concentration and adjusting the 3D printing process parameters.

When creating long-distance microchannels in bulk collagen, it is crucial to ensure that the soluble core material provides favorable support and solubility. We evaluated multiple options, including gelatin, Pluronic F127, and nanoclay. Our trials with gelatin and Pluronic F127 were met with difficulties. Gelatin failed to adhere sufficiently to collagen, and Pluronic F127 fell short in providing the needed support. As a result, we turned to nanoclay hydrogel, which dissolved effectively and did not possess the aforementioned shortcomings. To identify the optimal concentration of nanoclay, we developed a quantitative method for assessing its support[23] and solubility within the range of 4–8% w/w (2% interval, Figure 2H). Using the profile data of the cylindrical rings, the support was calculated using the proposed formula. Support is defined within the range [0, 1], with higher values indicating superior support. The dissolution rate was assessed as the weight percentage of the printed material dissolved in ultrapure water. We found that nanoclay at 8% achieved a support of 0.93 and a dissolution rate of 3.2% min^{-1}, which is appropriate for collagen bioprinting.

We successfully manufactured collagen grafts with high-density microchannels via multi-material bioprinting using the techniques described above (Figure 2I). The cross-sectional printed collagen grafts showed an excellent channel shape and accuracy (Figure 2L–N). We noted that the channel dimensions remained highly precise in the wet state, with a diameter of 154 μm (σ = 9.0 μm), which was close to the theoretical diameter of 160 μm. However, upon lyophilization, collagen contraction caused the channel size to increase to 217 μm (σ = 19.5 μm; Figure 2O), resulting in elevated porosity. We then tested the tensile modulus of the collagen grafts, which was 32.8, 130.1, and 133.7 kPa for concentrations of 4%, 5%, and 6%, respectively (Figure 2J). Next, we used the feature time (τ) of the exponential function to characterize degradation time (Figure 2K). The feature degradation time was 72.4, 97.0, and 123.2 h for concentrations of 4%, 5%, and 6%, respectively. Therefore, 5% collagen was selected for the remainder of the study because of its suitable mechanical properties and degradation behavior.

2.2. Precision Printing Model for NGF Gradients

Achieving a precise distribution of NGF gradients in collagen-based neural grafts is critical for effectively guiding long-distance nerve regeneration. In response to this challenge, we have devised a dual-component, motor-driven extrusion printhead (**Figure 3**A). This printhead accommodates pure collagen in one chamber, while the other contains a mixture of collagen and either NGF or pigment. This design enables us to control the concentration of NGF or pigment by manipulating the ratio between the two components, providing a potential range from 0% to 100%. We designed a terminal micro-nozzle with a 120 μm diameter channel and 120° confluence angle (Figure 3B). Theoretically, the extrusion volume should be directly proportional to the piston displacement, with differences attributed only to the conversion factor. However, the collagen hydrogel housed in the cartridge in reality exhibits significant viscoelastic properties, that is, the material has both viscous and elastic (compressible elasticity) characteristics. This introduces complexity in the mechanical transfer between the piston and nozzle. The compression generated by the displacement of the piston is absorbed by the elasticity of the collagen. In addition, the viscosity of collagen restricts its release over time, leading to a phenomenon known as transport relaxation.[18] This effect poses significant challenges to achieving accurate control of the extrusion volume. To overcome this issue, we developed a model-based approach to control the concentration gradients (Figure 3C). First, the continuously fluctuating concentration distributions were discretized. Next, we generated a control model employing a difference equation that incorporates the control parameter k. Specifically, when $k = 0$, there is no specific control, whereas $k > 0$ represents feedforward control through the derivative of the target quantity. This component of the model can be interpreted as the alteration prediction. Notably, this model is a simplified version of the dynamic model for the transport process.

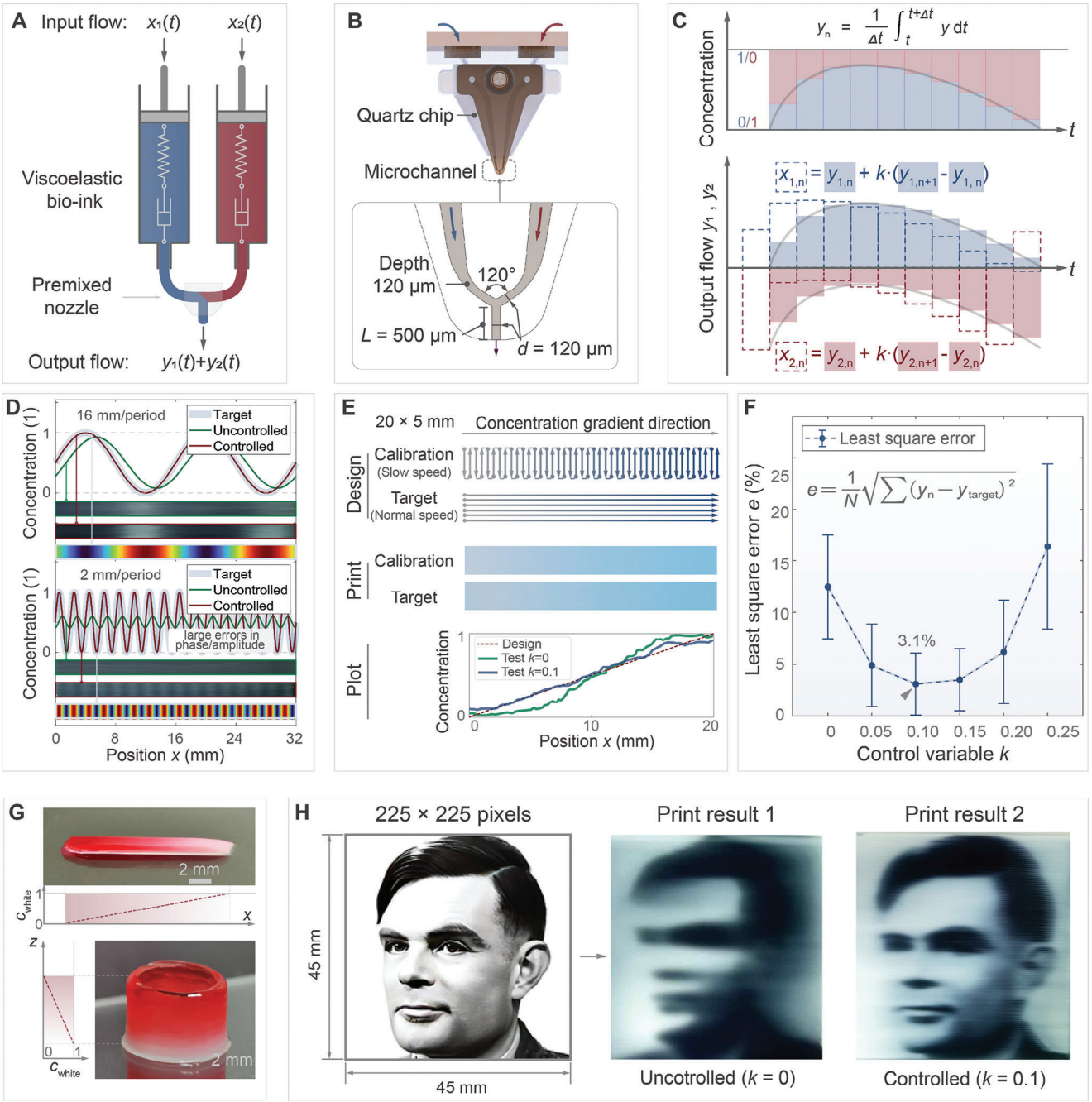

Figure 3. High-precision control model and performance of gradient printing. A) Schematic of the gradient print head structure showing the challenges in controlling the viscoelasticity of a large volume of collagen hydrogel ink. B) Nozzle structure design of the gradient printhead. C) Discretization method and control model schematic for gradient printing. D) Simulation curve of gradient printing at low and high spatial frequencies with actual printing effect. The higher the spatial frequency (resolution) of the print target, the greater the improvement obtained using the control strategy. E) Schematic and detection results of image calibration-based quantization detection method in gradient printing. F) Trend graph of gradient printing error under different control parameters. G) Printing effects of horizontal long bar and vertical cylindrical 3D structures. H) Grayscale photograph printing of a portrait of Alan Turing, demonstrating significantly improved accuracy of the concentration distribution before and after using the control strategy.

Model-based mathematical simulations and corresponding printing experiments were conducted at various spatial frequencies to evaluate the dynamic printing performance with and without the control model (Figure 3D). Spatial frequency serves as a pivotal metric in evaluating the performance of dynamic control within the domain of 3D printing. An elevated spatial frequency implies a higher count of ratio oscillations within an identical printing span, signifying superior precision in the printing process notably when intricate structures are involved. Our findings revealed that the error was relatively minor at lower

spatial frequencies (1/16 mm^{-1}), and the printing results displayed a clear sinusoidal pattern of light and dark patches, although amplitude and phase errors were present in the fully uncontrolled model (green line). In contrast, a significant error (≈80%) was observed at higher spatial frequencies (1/2 mm^{-1}), resulting in a printed image that was difficult to identify in terms of light and dark patches. At each frequency, the print result performed well, displaying a superior ability to that at 1/16 mm^{-1}. Overall, this study provides a control model that significantly enhances the dynamic performance and control accuracy of gradient printing.

To quantitatively assess the effectiveness of our gradient printing control technique, we proposed an automated concentration gradient detection method that relies on the photocalibration of print profiles (Figure 3E). This algorithm involves simultaneous printing of two linear gradients using different design trajectories and printing speeds. The slow low-spatial-frequency lines served as the calibration group, and the normal-speed high-spatial–frequency lines were designated as the target group to obtain a quantified gradient distribution curve. We then evaluated the control effect under a range of values of control parameter k and analyzed the least-squares error between the actual and target gradient curves (Figure 3F). The optimal control parameter value, which resulted in the smallest error (3.1%) and most favorable control outcome, was ≈0.1. By utilizing this approach, the optimal control model parameters for the ink could be quickly identified, thereby facilitating the quantitative characterization of the concentration gradient distribution.

Using the control approach and parameters outlined above, we successfully printed 3D structures incorporating linear gradients in both horizontal rectangular and vertical cylindrical formats (Figure 3G) using pigmented collagen ink. In cases of low spatial frequency, the printing speed could be increased to 20 mm s^{-1} without compromising the accuracy. We then printed a grayscale portrait of Alan Turing (pioneer in mathematical foundations of morphogenesis, Figure 3H) as an example of high spatial frequency and a complex pattern, using a 200 μm voxel and 45 × 45 mm format size. The digital model used to design the photograph was voxelized,[24] resulting in a 225 × 225 voxel framework. Our printing results, both before and after implementing the control strategy, clearly demonstrated a significant improvement in the accuracy of the concentration distribution.

2.3. Immobilization, Visualization, and Quantification of NGF Gradients in Collagen

To counteract the dissipation of soluble NGF and prevent the loss of the factor gradient, we utilized *N*-(3-dimethylaminopropyl)-*N*′-ethylcarbodiimide hydrochloride (EDC) and *N*-hydroxysuccinimide (NHS) to immobilize NGF onto collagen fibers, as shown in **Figure 4A**. These fibers, formed through the self-assembly of collagen under neutral conditions, have great potential as NGF carriers. The collagen fibers with immobilized NGF were dispersed in acidic collagen to create an NGF-loaded ink. However, crosslinking can lead to the agglomeration of collagen fibers, which was attributed to the reduced hydrophilicity caused by the consumption of amino and carboxyl groups during crosslinking. To maintain favorable dispersion properties of the collagen fibers after crosslinking, we integrated the polysaccharide heparin, which has abundant carboxyl groups, into the crosslinking system to enhance the hydrophilicity of the fibers. Our findings indicate that introducing heparin into collagen fibers resulted in comparable levels of scale and dispersibility to those observed before crosslinking and after immobilization. To validate the effectiveness of this method, we devised a fluorescence-based visualization assay (Figure 4A). For this assay, we labeled collagen fiber carriers with fluorescein 5(6)-isothiocyanate (FITC, green) and used immunofluorescence (Cy3, red) to visualize the location of NGF. Figure 4B shows that the fluorescence signals from FITC-labeled collagen fibers and NGF immunofluorescence overlapped entirely, thus confirming the efficacy of this approach.

To validate the accuracy of NGF concentration printing, we bioprinted five collagen blocks under steady-state conditions with concentrations ranging from 50 to 250 pg mL^{-1} at intervals of 50 pg mL^{-1} without crosslinking and subjected them to an enzyme-linked immunosorbent assay (ELISA). The soluble NGF concentrations were directly proportional to the optical density obtained by ELISA (Figure 4C, blue line), with a high correlation coefficient of $R^2 = 0.981$. Furthermore, we used collagen with a fluorescent carrier for NGF to create the same structure and compared the NGF concentration to the fluorescence intensity of the acquired images (red line). Our results demonstrated that the NGF concentrations were directly proportional to the image intensity, with an extremely high correlation coefficient of $R^2 = 0.996$, highlighting the ability to utilize fluorescence intensity to accurately characterize NGF concentrations (Figure 4C). Additionally, we conducted two experiments involving NGF gradient printing and quantification (Figure 4D) utilizing linear and quadratic distributions, respectively, based on the observed linear correlation between the NGF concentration and image intensity. The root mean square error (RMSE) for the design curve and the curve obtained from the image was 18.72 and 26.58 pg mL^{-1}, respectively. The RMSEs were relatively small, providing compelling evidence for the high accuracy of the current NGF gradient printing techniques.

2.4. In Vitro Model: Quantitative Characterization of Neurite Guidance

In vitro models are paramount in cell biology research given their capacity to facilitate conclusive findings via quantifiable and readily observable cellular experiments.[25] We devised four distinct in vitro models utilizing collagen-based substrates to culture single neurons or dorsal root ganglion (DRG) explants, which are well-characterized models for investigating the bio-effects of structures and biological factors. These models consisted of non-structured, non-NGF, uniform NGF (U-NGF), and gradient NGF (G-NGF) models, with the latter three models incorporating microgrooves on their surfaces (160 μm groove width, consistent with the diameter of the neural graft channel; **Figure 5A**). Following a 72 h incubation period of DRG explants on the four samples, we conducted β-tubulin immunofluorescence staining to visualize the DRG morphology (Figure 5B). The DRG axon direction statistics (Figure 5C) was acquired using image-processing algorithms, with the density distribution fitting an elliptical contour.

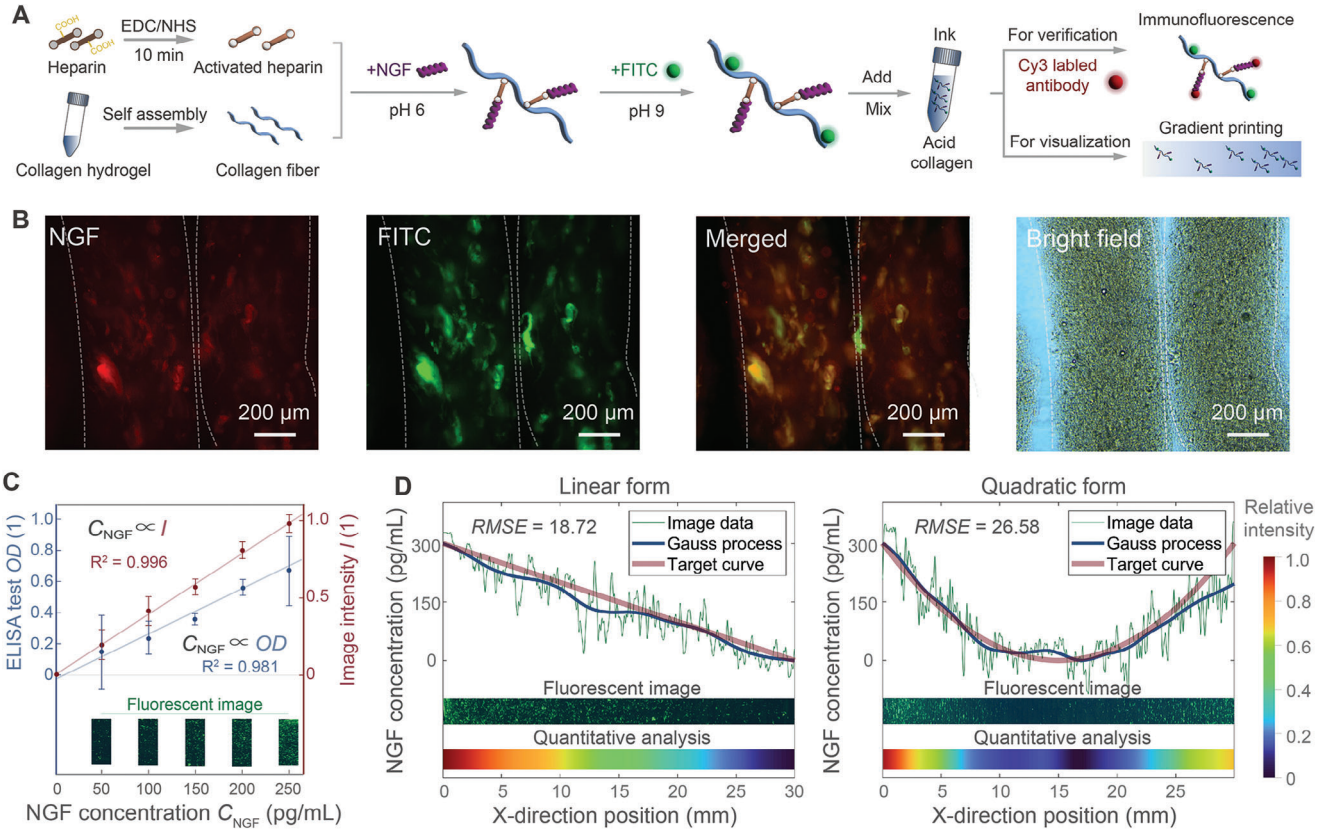

Figure 4. Immobilization and visualization of NGF on collagen. A) Crosslinking collagen fibers with NGF, and visualization of the method using green fluorescence (FITC) to label collagen and red fluorescence (Cy3) to label NGF. B) Calibration photos of collagen fibers with NGF, demonstrating their spatial overlap. C) Comparison of actual NGF concentrations obtained by the enzyme-linked immunosorbent assay (ELISA) method and image data, showing good linear correspondence ($n = 3$). D) Gradient printing of concentration distribution curves in linear and quadratic forms with quantification of concentrations using fluorescence images. Notes: OD, optical density; *I*, image intensity; RMSE, root mean square error.

Statistical analysis of the DRG axon lengths (*L*) for different test models showed that the regeneration lengths of the four models increased to different extent (Figure 5D). The DRG explants seeded on the G-NGF group exhibited longer axons (1.80 ± 0.13 mm) than those on the U-NGF (1.52 ± 0.15 mm), non-NGF (1.34 ± 0.10 mm), and non-structured (0.64 ± 0.05 mm) groups. In the presence of the G-NGF group, the average length of the neurites on the high-NGF concentration side was 1.7 times longer than that on the low-NGF concentration side, which was not observed in the remaining groups. Based on the fitted ellipse, the anisotropy (An) was computed to clearly ($p < 0.001$) show the effect of structural guidance (Figure 5E). We employed asymmetry analysis based on an ellipse to characterize DRG growth asymmetry (As) and quantify the impact of chemical guidance on regeneration. Our results clearly demonstrated that chemical guidance had a significant ($p < 0.001$) effect on DRG growth asymmetry (Figure 5F). Compared to the guidance ratio defined by a nonzero number of pixels in a fluorescent image,[14,25,26] our evaluation method is less susceptible to experimental chance, and thus provides more robust results.

In addition, we developed a quantitative index, regeneration guidance length (*G*), to evaluate the efficacy of different in vitro models in promoting regeneration guidance (Figure 5G). This measure is based on the analysis of neuron growth length *L*, anisotropy An, and asymmetry As, allowing for a comprehensive assessment of the regenerative potential of each model. In this part, Schwann cells (SCs), the vital glia cells which support axon elongation in peripheral nerves, were seeded onto the various models (Figure S5B, Supporting Information) and their elongated lengths were recorded (Figure S5C, Supporting Information). A similar trend to that observed for the DRG explants was observed. For a comprehensive analysis, we conducted additional experiments involving the cultivation of SCs and measured their apoptosis rates in various models using flow cytometry (Figure S5D–E, Supporting Information). Notably, all measured apoptosis rates were minimal, further confirming the biocompatibility and safety of the in vitro models. In summary, we introduced a novel in vitro model to evaluate both structural and chemical guidance for nerve regeneration. Specifically, anisotropy was used to assess the impact of structural guidance, whereas asymmetry was used to evaluate the effects of chemical guidance.

2.5. In Vivo Animal Model: Nerve Graft Enhance Peripheral Nerve Regeneration

For potential therapeutic applications in nerve regeneration medicine, it is crucial to demonstrate whether a combination of

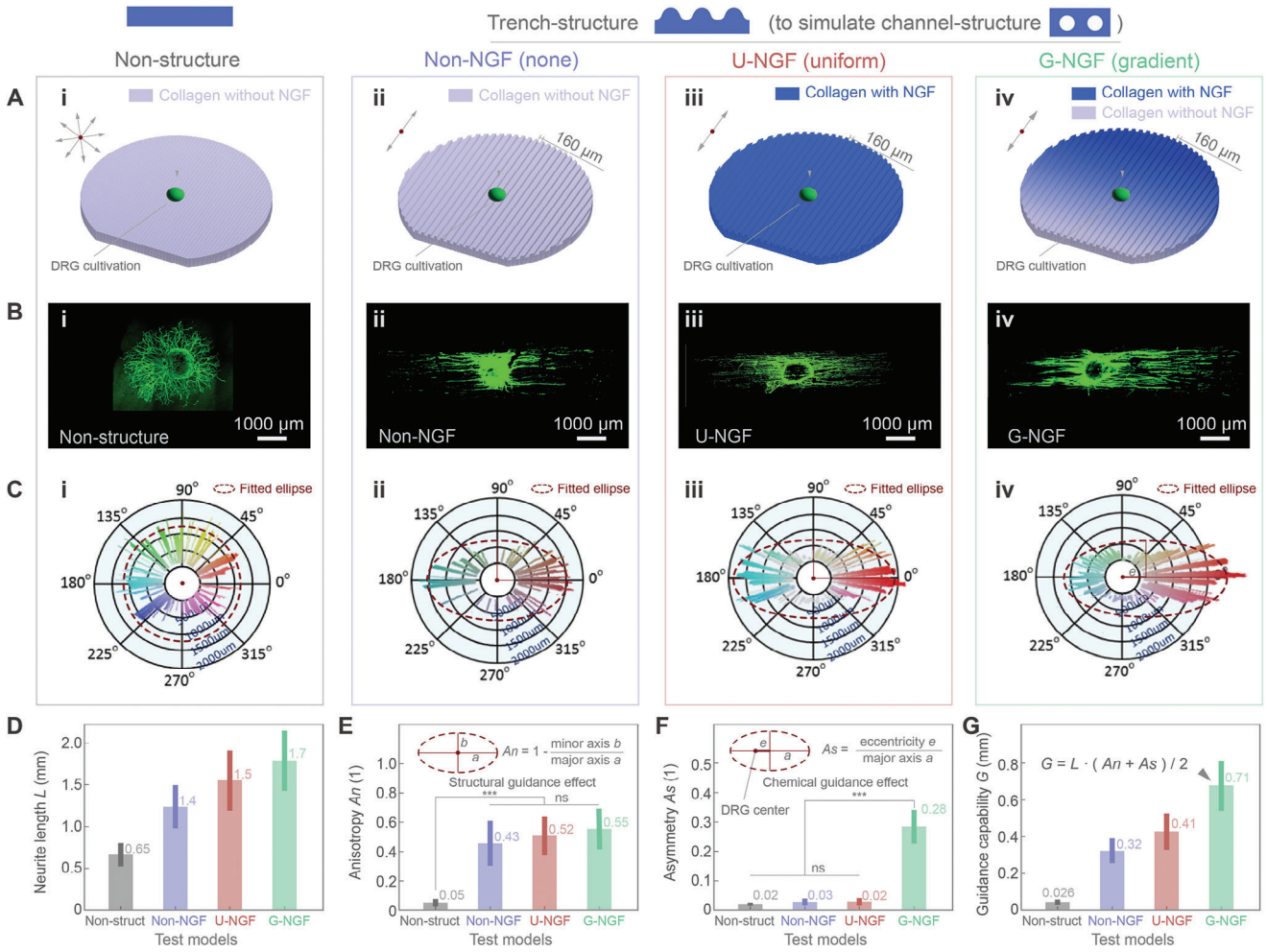

Figure 5. Visualization experiments of cellular cultivation morphologies of collagen structures with different surface morphologies and NGF components to quantify the roles of structural and chemical guidance in neural regeneration. A) Design and printing of experimental samples with structures and components, including non-structure, non-NGF, uniform NGF (U-NGF), and gradient NGF (G-NGF). B) Example photos of DRG growth morphology on different sample surfaces. C) Density distribution of DRG axon direction statistics under different test models, which can be fitted to an elliptical contour. D) DRG axon length statistics under different test models. E) Anisotropy, calculated based on the fitted ellipse, is used to characterize the structural guidance effect. F) Eccentricity based on the ellipse is used to characterize the asymmetry of DRG growth, reflecting the chemical guidance effect of the sample for regeneration. G) Based on the neural growth length, anisotropy, and asymmetry, a regeneration guidance length is designed to characterize the regeneration-guiding capacity of the material. Data are presented as mean ± standard deviation and statistically evaluated by one-way ANOVA. ***, $p < 0.001$.

oriented topographical cues and biochemical gradients can promote nerve regeneration in vivo. The nerve graft was used to repair a 15 mm sciatic nerve defect. Twelve weeks after surgery, the nerve segments were immunostained (**Figure 6**A). The regenerated axons were distributed evenly in the G-NGF groups, which were superior to those in the U-NGF and non-NGF groups, with more NF-160 positive axons and S-100 positive SCs in the G-NGF group (Figure 6A,B). To morphologically evaluate nerve regeneration, the harvested nerves were stained with methylene blue. The number of myelinated axons in the G-NGF group was significantly higher than that in the U-NGF and non-NGF groups (Figure 6C,D). The remyelination of the regenerated axons was further assessed using transmission electron microscopy (TEM). The thickness of the myelin sheath in the G-NGF group was significantly greater than in the U-NGF and non-NGF groups (Figure 6C,D). As another important indicator of the remyelination of regenerated axons, the *G*-ratio (axon-to-fiber ratio) was significantly lower in the G-NGF group than in the U-NGF and non-NGF groups ($p < 0.05$, Figure 6D), suggesting that a high degree of remyelination was achieved by G-NGF.

The function and structure of the gastrocnemius muscle are essential indicators of the extent of sciatic nerve regeneration. The bilateral gastrocnemius muscles were harvested and weighed 12 weeks after surgery (**Figure 7**A). Masson's trichrome staining revealed atrophy of the gastrocnemius muscles in the G-NGF (922 ± 9.6 μm^2), which was significantly greater than that in the U-NGF (908 ± 10.5 μm^2) and non-NGF (867 ± 29.4 μm^2) groups ($p < 0.05$, Figure 7B). In addition, the muscle wet weight

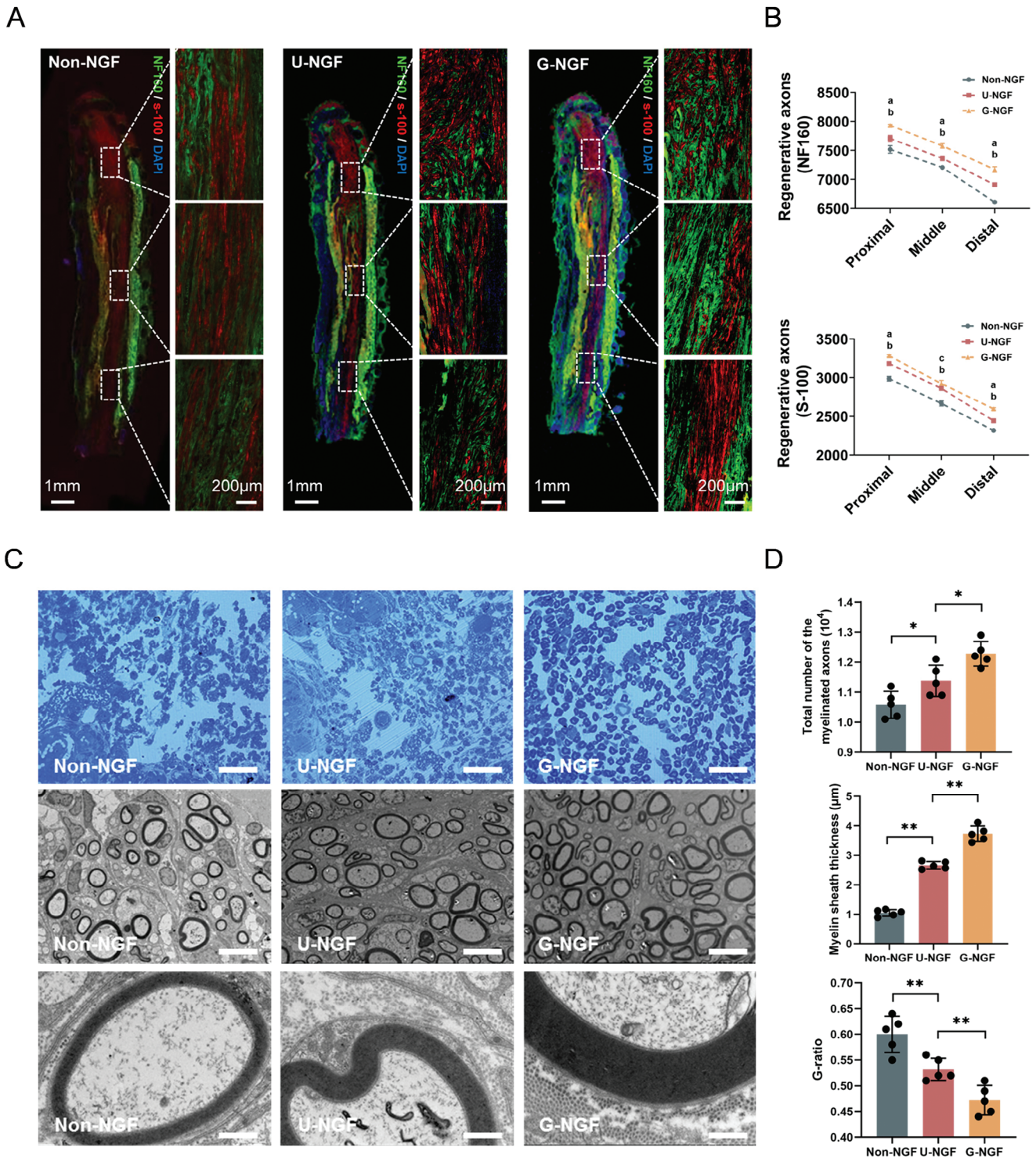

Figure 6. In vivo experiments for promoting nerve regeneration. A) Immunofluorescence staining of nerve transverse section 12 weeks after operation (green is NF-160–labeled regenerated axons, red is S-100–labeled SCs, blue is 4′,6-diamidino-2-phenylindole solution). B) Immunofluorescence staining of the nerve transverse region divided into three sections (proximal, middle, and distal) to count the number of regenerated axons and SCs of different graft types. C) Representative images of methylene blue by transmission electron microscope 12 weeks after surgery. D) Number of myelinated axons, thickness, and *G*-ratios in the distal portion of the neural graft. Data are presented as mean ± standard deviation and statistically evaluated by one-way ANOVA. *, $p < 0.05$; **, $p < 0.01$.

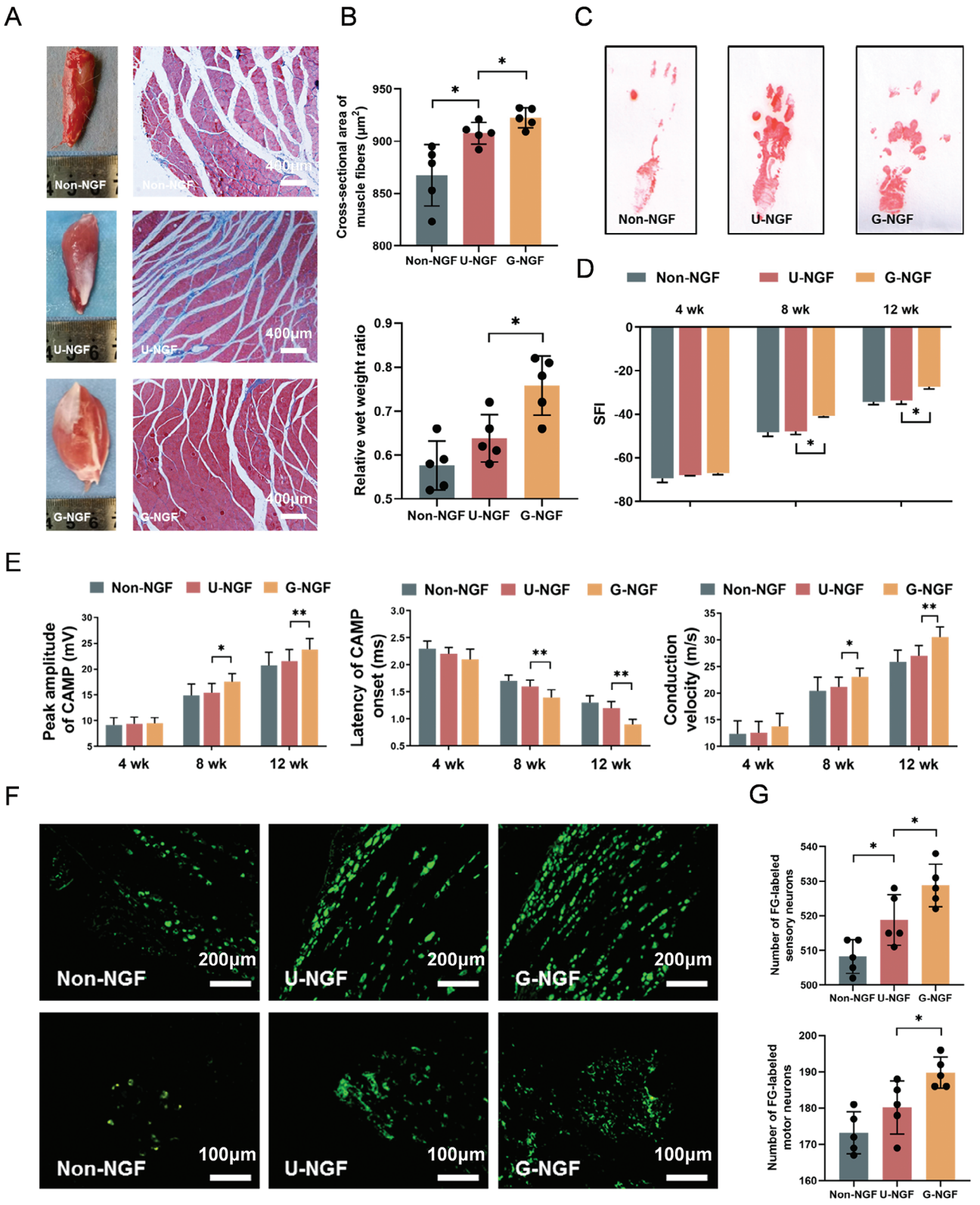

Figure 7. In vivo experiments for promoting nerve function. A) Representative images and Masson's trichrome staining of the gastrocnemius muscle 12 weeks after surgery. B) Statistics of the muscle wet weight ratio and muscle fiber cross-sectional area based on gastrocnemius images. C) Walking track analysis following surgery. D) Statistics of sciatic functional index (SFI). E) Electrophysiological examination after surgery. F,G) FluoroGold (FG)-labeled positive sensory neuron and motor neuron photos and statistics 12 weeks after surgery. Data were presented as mean ± standard deviation and statistically evaluated by one-way ANOVA. *, $p < 0.05$; **, $p < 0.01$.

ratio of the G-NGF group (0.75 ± 0.07) was significantly higher than that of the U-NGF (0.64 ± 0.05) and non-NGF (0.58 ± 0.06) groups ($p < 0.05$, Figure 7B).

Loss of nerve innervation and muscle atrophy induces morbid gait in rats. Walking track analysis was performed every 4 weeks following surgery to assess the restoration of motor function (Figure 7C). The sciatic functional index (SFI) was calculated from the footprints to assess the sciatic nerve function. An SFI value approaching zero indicates normal motor function, whereas an SFI value approaching −100 denotes total loss of function. The SFI values decreased to a relatively low level in the initial 4 weeks after surgery in all groups, indicating the onset of muscle denervation and motor dysfunction caused by nerve transection. At 8 and 12 weeks, the corresponding SFI values in the G-NGF group were significantly higher than those in the U-NGF and non-NGF groups.

The goal of peripheral nerve regeneration, particularly for long-term nerve abnormalities that require a long time to regrow, is to restore nerve conduction and motor function. Electrophysiological examination was performed, and the compound muscle action potential (CMAP) index was obtained to assess the recovery of nerve conduction. As displayed in Figure 7E, the CMAP amplitude at the injured side at 12 weeks in the G-NGF group (23.8 ± 2.1 mV) was significantly higher than that in the U-NGF (21.6 ± 2.2 mV) and non-NGF (20.7 ± 2.6 mV) groups. The CMAP latency was statistically shorter in the G-NGF group (0.92 ± 0.09 ms) than in the U-NGF (1.45 ± 0.14 ms) and non-NGF (2.13 ± 0.19 ms) groups. In addition, the conduction velocity was faster in the G-NGF group (30.5 ± 1.9 m s^{-1}) than in the U-NGF (23.1 ± 1.6 m s^{-1}) and non-NGF (13.8 ± 2.4 m s^{-1}) groups. These results suggest that grafts with both structural and chemical guiding cues significantly accelerated neurological functional recovery after nerve repair.

A retrograde tracer analysis was performed to further examine the extent of the regenerated axons growing across the nerve defect. As shown in Figure 7F,G, the numbers of FG-labeled motor neurons in the ventral horn of the spinal cord and FG-labeled sensory neurons in the DRG in the G-NGF group were significantly higher than those in the U-NGF and non-NGF groups. This suggests that the axons of both the sensory and motor neurons were successfully regenerated across the defect and reached their target destination after treatment with the G-NGF graft.

3. Discussion

This study introduced a quantitative biofabrication platform specifically for constructing collagen-based peripheral nerve grafts that incorporate both structural and chemical guidance. By developing a computable viscoelastic model for collagen hydrogel and a gradient printing control model for NGF distribution, we successfully fabricated a sophisticated nerve graft that effectively promoted the linear growth of axons both in vitro and in vivo. This study offers a versatile platform for precise collagen printing that clarifies the biofabrication of collagen-based tissues and organs requiring meticulous structural and biochemical cues.

Collagen bioprinting techniques have been greatly improved to address the challenging soft properties of collagen.[20] The freeform reversible embedding of suspended hydrogels (or "FRESH") printing technique extends the capabilities of extrusion bioprinting by utilizing a rapid pH change to induce collagen self-assembly in a buffered support bath, thereby significantly reducing the formation time of collagen filaments and improving printing accuracy.[3] Additionally, light-based bioprinting of norbornene-functionalized neutral-soluble collagen[27,28] has demonstrated adequate mechanical strength during the 3D formation process, leading to enhanced final shape fidelity and expansion of the range of applicable ink viscosities. In this study, we performed direct printing of high-concentration acidic collagen ink, which required a comprehensive understanding and accurate prediction of collagen relaxation dynamics. To achieve this, we developed an analytical model of collagen hydrogels to calculate their deformation behaviors. This model also provides a quantitative analytical technique for the embedded and light-based printing of collagen, potentially explaining the physical mechanisms underlying 3D collagen assembly. Furthermore, based on principles linking molecular parameters and macroscopic properties,[29] viscoelastic models can serve to link rational material design and desirable printing effects.

Soluble core materials, distinct from traditional sacrificial materials, are specifically engineered to dissolve and create intricate microchannels within bioprinted constructs such as peripheral nerves and vascularized tissues.[18] Therefore, ideal soluble core materials have more requirements than sacrificial materials. First, they should possess a higher yield strength than the bulk material to avoid distortion caused by the compression of the bulk filaments. Second, they should be compatible with the bulk material to prevent physical or chemical reactions that could compromise the structural integrity. Finally, they should be easily removed to minimize any residue remaining within the microchannels.[30] We evaluated the most commonly used sacrificial materials reported in the literature. For example, carbohydrate glass[31] displays sufficient stiffness and rapid dissolution but undergoes significant changes upon contact with water in collagen hydrogels during the printing process. Pluronic F127 can be quickly liquefied at low temperatures and dissolve conveniently in aqueous media.[24] Additionally, it has low strength and undergoes dehydration when combined with acidic collagen hydrogels, resulting in filament instability. Gelatin, which has been shown to be a suitable soluble core material for bulk GelMA (methacrylated gelalin),[32] is mechanically weak, leading to filament distortion and channel blockage. Although the utilization of nanoclay hydrogels as soluble core materials has rarely been reported, nanoclay hydrogels offer certain advantages. First, when nanoclay is introduced at concentrations exceeding 2% w/w, it forms a reversible "house-of-cards" nanostructure through electrostatic interactions between the negatively charged surface and positively charged edge of the 2D nanoparticles. This property renders nanoclay a typical Herschel–Bulkley fluid with high yield strength, shear-thinning behavior, and rapid recoverability for high-fidelity extrusion.[24] Second, nanoclay is inert to acidic collagen, and their compatibility is further ensured by the temperature-insensitive characteristics of the nanoclay. Third, nanoclay exhibits the convenient ability to dissolve mildly in ultrapure water. Therefore, we ultimately selected nanoclay as the soluble core material for collagen nerve graft printing. However, it is important to note that for smaller microchannels, specifically those with a diameter under 100 μm, the solubility of nanoclay needs further improvement, especially for potential

applications in vasculature bioprinting. In addition to its rheological properties, nanoclay possesses thermal stability, optical transparency, and ionic insensitivity compared to commonly used sacrificial materials, making it a promising functional support bath material for embedded bioprinting.[33]

Natural tissues exhibit a diverse range of spatial gradients, as exemplified by the polarized neural tube during embryonic development and the osteochondral interface found at articulating joints.[34] Functionally graded materials (FGMs), characterized by gradual variations in composition and structure throughout their volume, have the potential to mimic biological gradients, encompassing features such as porosity, fiber alignment, strength, and cell signaling.[35] Moreover, FGMs have attracted significant interest in various non-biological domains, including aerospace engineering, the automotive industry, optoelectronic devices, and the energy sector. Consequently, fabrication methods for gradient materials have become a central focus in both biological and non-biological manufacturing. Among these methods, 3D printing has emerged as an exceptionally effective technique, encompassing various approaches such as digital light processing,[36] inkjet printing,[37] and extrusion-based printing.[38,39] Extrusion-based printing offers notable advantages in biomanufacturing owing to its cell-friendly nature, adaptability to diverse ink types, capacity for multi-material dispersion, and straightforward configuration. However, gradient printing through extrusion-based approaches is impeded by limited accuracy, particularly at low spatial frequencies.[39] This limitation stems primarily from the lack of an effective understanding and control model for viscoelastic bio-ink extrusion. To address this issue, a microfluidic circuit analog model for gradient printing is proposed.[40] Nonetheless, this approach transposes mechanical issues into electrical ones, thereby obscuring the model's physical significance in a succinct and intuitive manner. Consequently, its applicability and precision are comparatively suboptimal. In this study, we adopted a distinct modeling perspective. Specifically, we revealed that the relaxation phenomenon occurs during the transport process of viscoelastic inks[18] and proposed a comprehensive dynamic model. Using this mechanical model, we derived and simplified the core equations, resulting in the single-parameter model presented in this study. Combined with an image calibration method based on the proposed printing patterns, this model enables the rapid determination of optimal parameter values tailored to different inks and printing conditions, thus enhancing both efficiency and user-friendliness. By leveraging our control model, we demonstrated high-precision extrusion-based gradient bioprinting at high spatial frequencies. This methodology also has the potential to be seamlessly integrated into structural gradient designs, offering an effective and user-friendly solution for fabricating biological gradient tissues and FGMs.

3D printing is a digital manufacturing technology that relies heavily on design software. In the context of bioprinting tissues and organs, the intricate internal structures and specific spatial distributions of materials present significant challenges in digital design methodologies.[41] Voxel-based design and printing methodologies have gained significant attraction in inkjet printing[37] and digital light processing.[42] Recently, the concepts of voxelated[43] and subvoxel[44] printing have been introduced for the extrusion-based processing of soft materials. In our previous study, we developed a voxel-based digital model that integrates and manages multidimensional information to effectively address the complexities associated with the multi-material interface.[24] In this study, with a focus on the design and fabrication of factor gradient neural grafts, we expanded this framework by referring to it as a voxel-rich model that simultaneously incorporates the proportion of material components and control model formulas within each voxel. This model-driven approach allows us to deliberately design the structure and material distribution of neural grafts while accurately aligning the control model parameters to achieve precise extrusion. By integrating both the target and process spaces, the expanded voxel-rich model facilitates the convenient design and efficient control of bioprinting. This advancement has substantially broadened the horizons of possibilities in biological tissue design and manufacturing.

Local delivery of growth factors encompasses two primary strategies: non-covalent immobilization and covalent conjugation. Currently, non-covalent immobilization is recognized as a promising approach, owing to its stability and enduring efficacy.[45] Conjugation techniques rely on the presence of functional reactive groups in both the substrate and growth factor structure, the relative positioning of these groups within the growth factor molecules, and their correlation with the receptor-binding regions.[46] Covalent conjugation employing EDC/NHS has exhibited favorable biological effectiveness for NGF.[47,48] However, when NGF is directly coupled to collagen, non-selective crosslinking strategies, such as EDC/NHS, can significantly impede the solubility and printability of collagen. To address this concern, an alternative approach is proposed in this study to incorporate NGF-loaded fibers into printing materials by conjugating NGF with collagen fibers. We employed self-assembled collagen fibers as a cost-effective and readily obtainable immobilization substrate. Notably, our focus was primarily to assess the applicability of this method to NGF, and further investigations are required to evaluate its suitability for other types of growth factors. For covalently conjugated growth factors, the accurate quantification of their concentrations poses a challenge. Fluorescence labeling methods are typically used to visualize the localization or gradient distribution of growth factors.[49,50] In this study, we utilized image processing techniques to capture and analyze NGF printing gradient, which allows for investigating the role of variable-gradient signaling molecules in 3D matrices, thus helping to better understand their role in tissue regeneration.

Using the present techniques and methodologies, we successfully engineered collagen-based peripheral nerve grafts that incorporate a customizable NGF gradient into microchannel structures. Through the integration of chemical and structural cues, our graft demonstrated remarkable efficacy in promoting neurite outgrowth, which was validated by favorable outcomes observed both in vivo and in vitro. Our biofabrication platform introduces a comprehensive framework that encompasses a quantified design, processing, and evaluation. Consequently, it ensures the consistent quality of individual grafts, with reproducibility and consistency being fundamental for future endeavors aimed at commercialization. Moreover, our platform accommodates personalized design and fabrication[18] specifically tailored to a diverse range of neural injury cases and effectively addressing the unique needs of patients. This approach has immense potential to deliver differentiated value-added products and services,

thereby empowering medical institutions to meet a broader spectrum of demands.

Our framework possesses exceptional capabilities for the precise construction of bionic microstructures and the accurate distribution of material components, establishing it as a versatile universal biofabrication platform for collagen-based materials. Furthermore, it offers a highly adaptable design capacity and quantitative evaluation framework tailored for tissue engineering. Consequently, our platform has not only achieved successful fabrication of high-density multi-channel collagen grafts with an NGF gradient for peripheral neural regeneration, but also exhibits significant potential for applications in diverse tissues and organs, including the liver, heart, and kidney. The reproducibility and customization inherent in this manufacturing technique have promise as a valuable tool in various domains of biomedical research, including axon guidance, vascular development, and spatiotemporal cell biology.[25] Despite the progress achieved with our manufacturing platform, certain limitations require further investigation. Our bioprinting processes are intricately connected to the specific properties of collagen, and therefore may encounter challenges when incorporating other components of the ECM, such as polysaccharides.[18] Additionally, a balance between speed and accuracy emerges when considering multi-material bioprinting. The fundamental principle of 3D printing involves the discrete deposition and subsequent reassembly of materials. Enhancing the precision of material discretization often results in a reduced assembly speed, as it is constrained by the physical systems governing the material distribution. To overcome this challenge, pursuing innovative engineering designs, such as large-scale parallel processing systems, represents a promising avenue.[18]

4. Conclusion

This study presents a pioneering biofabrication platform for collagen-based peripheral nerve grafts, which integrates bionic structural and chemical guidance cues in a quantifiable manner. To achieve this, we developed a computable viscoelastic model for collagen, allowing us to accurately predict its transient behavior and fabricate neural grafts consisting of 24 longitudinal channels within a 2 mm diameter, faithfully replicating the intricate architecture of native peripheral nerves. In addition to the structural aspect, we developed a gradient printing control model and implemented a visual quantitative method to ensure the precise distribution of NGF within the collagen matrix. Through comprehensive validation procedures involving both in vitro and in vivo studies, we evaluated the efficacy of our peripheral nerve graft in guiding axonal growth. This universal biofabrication strategy, which employs a one-step bioprinting process that integrates structural and chemical cues, has great promise for the fabrication of nerve grafts and paves the way for various tissue and organ manufacturing applications in tissue engineering and regenerative medicine.

5. Experimental Section

Bio-Ink Preparation: i) Collagen bio-ink was prepared using type I collagen sponge (Shiji Kangtai Biomedical Engineering Co., Ltd., Tianjin, China) immersed in 1% v/v acetic acid, left to stand for 48 h at 4 °C with sufficient agitation until the collagen was fully dissolved, and then centrifuged at 10 000 r min^{-1} for 1 h to remove air bubbles. ii) The soluble core material was made of laponite nanoclay (Yiwei Tehua Co., Ltd., Beijing, China). The powder was mixed with pure water by thorough shaking and stood at 25 °C for 24 h. The material was used once it was transparent.

Creep Testing and Parameter Identification: Using the creep-reversion mode of a rheometer (RST-CPS; AMETEK Brookfield, Middleboro, MA), a 60 s creep and 60 s recovery setting was used for material concentrations corresponding to different concentrations of collagen, and the constant stress applied during creep was appropriately adjusted owing to their different yield strengths (Figure S1, Supporting Information). A program was written in MATLAB (MathWorks, Natick, MA) to identify the four parameters (G_1, G_2, η_2, and η_3) in the functional equation using the least squares method. The functional equation that represents the creep response of the Burgers model was as follows

$$\gamma(t) = \begin{cases} \frac{\sigma_0}{G_1} + \frac{\sigma_0}{G_2}\left(1 - e^{-tG_2/\eta_2}\right) + \frac{\sigma_0}{\eta_3}t \ (t \le t_0) \\ \frac{\sigma_0}{G_2}\left(1 - e^{-t_0G_2/\eta_2}\right)e^{-(t-t_0)G_2/\eta_2} + \frac{\sigma_0}{\eta_3}t \ (t > t_0) \end{cases} \quad (1)$$

Bioprinting Method: Experiments were performed using a self-developed bioprinter, SIA Bioprinter PRO, and the printer photo and hardware configuration were as shown in Figure S3 (Supporting Information). The printer had five multifunctional stations, each with electric, pneumatic, and dual-stage temperature controls. The design software was BiopDesigner 8.3.0, a special design software configured for the printer, which enabled the concentration gradient setting function and provided a control model for viscoelastic materials.

Quantitative Characterization of the Supportability of Soluble Core Materials: A mathematical characterization-based method was designed for quantitative fidelity evaluation. For each concentration of soluble core materials, the same cylindrical tubular printing program was used with height $L = 10$ mm to extract the outer profile to quantitatively calculate and analyze its fidelity. Fidelity was defined as

$$f = e^{-\frac{1}{L}\int_0^L |x| dx} \approx e^{-\frac{1}{N}\sum |x_n|} \quad (2)$$

where x represents the difference from the average vertical line.

For approximation, the curve can be divided equally into N segments and the Riemann sum can be used instead of integration. Such a definition had three advantages: i) the closer the result was to the design, the higher the fidelity, which was one at the closest and tends to zero at the furthest; ii) when the print height cannot be the same as that achieved with the design, then the fidelity can be directly obtained as zero by definition; iii) the infiltration of different materials can be compared, and information on the infiltration can be obtained by setting $\Delta L = L/N$ to be smaller than the layer height.

Quantitative Characterization of Solubility of Soluble Core Materials: Printed structures of nanoclay materials with different mass fractions were immersed in pure water and removed every 3 min. Excess water was removed with absorbent paper and weighed, and the recorded values were plotted as a curve (Figure S2, Supporting Information). A dissolution of 50% was set as the characteristic point of dissolution to calculate the dissolution rate of the soluble core material.

Quantification of Mechanical Properties of Neural Grafts: A texture analyzer (CT3-100; AMETEK Brookfield) was used to test the tensile modulus of the neural graft at room temperature with a trigger point load of 0.008 N and test speed of 0.25 mm s^{-1}. A strain rate of <0.04 was used to fit a line, and the slope of this line was the tensile modulus. The grafts with different collagen concentrations were first placed in pure water for 1 h to ensure removal of the swelling effect, then placed in type I collagenase solution with an activity of 20 unit per mL, placed in a 37 °C cell incubator, and weighed every 8 h. The degradation curves were obtained by normalizing the initial mass to the unit mass.

Gradient Printing Method with Quantitative Assay: The two-component print head of the SIA Bioprinter PRO was used (Figure S3, Supporting Information), and collagen ink with and without NGF was added to the two bins. A standard gradient printing calibration algorithm was provided in the BiopDesigner software, which was used to obtain the gradient printing accuracy for specific control parameters. The calibration algorithm was based on the principle of printing both quasi-static and dynamic gradient models, taking pictures under identical lighting conditions and using quasi-static pictures as the calibration standard to obtain the dynamic gradient values (Figure S4, Supporting Information).

Preparation of Collagen Fibers: Collagen I from bovine tendon was dissolved in 0.08 M acetic acid to obtain 0.3% w/v homogeneous solution at 4 °C. Acidic collagen was adjusted to pH 7.0 with 1 M NaOH and 10× Dulbecco's modified Eagle's medium, and immediately placed in an incubator. After 30 min, the assembled collagen hydrogel was disrupted using a homogenizer. After 10 000 r min^{-1} centrifugation for 10 min, collagen fiber precipitation was obtained, which was then washed and centrifuged three times with 2-(*N*-morpholino) ethanesulfonic acid buffer (MES; pH 6, 0.1 M).

Binding NGF and Fluorescent Groups on Collagen Fibers: To activate the carboxyl group in heparin, EDC (30 mM) and NHS (15 mM) were added to heparin sodium (1% w/v, 20 mL) in MES buffer (0.1 M, pH 6) for 10 min. Then, 5 µg of NGF was added to the activated solution for 30 min. Collagen fibers from 30 mL of acidic collagen were added under stirring for 12 h. After three instances of washing and centrifugation with sodium bicarbonate solution (pH 9, 0.1 M), the fibers were mixed with 50 mL of sodium bicarbonate solution. Fifty microliters of FITC (50 mg mL^{-1}) were added to the mixture and stirred in the dark for 12 h. Collagen fibers with bound NGF and fluorescent groups were obtained after three washes with phosphate buffered saline (PBS).

Staining of Collagen Fibers: The NGF collagen fibers and collagen solution were mixed in a ratio of 1:4, and then extruded into 37 °C PBS to form collagen filaments. The collagen filaments were fixed with 4% paraformaldehyde for 2 h at room temperature. The filaments were then washed twice with Dulbecco's PBS (D-PBS) for 10 min. After being blocked by 3% bovine serum albumin in D-PBS for 60 min, the filaments were incubated with goat anti-human β-NGF antibody (R&D Systems, Minneapolis, MN) at 4 °C for 18 h, washed three times with D-PBS, and then incubated with Cy3-conjugated secondary antibody for 2 h at room temperature in the dark.

NGF ELISA: To further verify the gradient distribution of NGF, gradient printing was performed using collagen mixed with 50 mg mL^{-1} NGF and collagen without NGF. After printing was completed, the graft was quickly cut into five parts (≈25 mg per part) and soaked in 1 mL of PBS at 4 °C overnight. The absolute value of NGF in each section was measured using an NGF ELISA kit (R&D Systems).

Isolation and Characterization of SCs: Primary cultures of SCs were collected from the sciatic nerve and brachial plexus of newborn (P1-2) Sprague Dawley (SD) rats (provided by the Fourth Military Medical University Animal Center). All experimental procedures were conducted in accordance with the guidelines of the Laboratory Animal Care and Use (Publication No. 85-23, 1985) of the National Institute of Health and were approved by the Animal Research Committee of the Fourth Military Medical University of the People's Republic of China. Double immunofluorescence staining was performed on primary cultures of SCs using S100 protein antibody (ab52642; Abcam, Cambridge, UK). Nuclei were stained with 4′,6-diamidino-2-phenylindole solution (Sigma-Aldrich, Burlington, MA). Primary cultures of SCs were not passaged more than three times.

Preparation of DRG Explants and Neuronal Cultures: To better visualize neural protrusion growth and alignment, DRG explants from neonatal rats were isolated and cut in half. The cut surface was placed directly on the surface of the longitudinal section of the graft, preserved in a medium supplemented with 50 ng mL^{-1} human nerve growth factor (R&D Systems), 2 mM L-glutamine (Thermo Fisher Scientific Inc., Waltham, MA), 2% B27 (Thermo Fisher Scientific), and 1% penicillin–streptomycin in neural basal medium (Thermo Fisher Scientific). The DRG explants were incubated for 3 days and fixed with 4% paraformaldehyde. Immunostaining of the samples was performed. The following primary antibodies were used: mouse anti-β-microtubulin III (1:200; Abcam) and goat anti-mouse Alexa 488 (1:500; Thermo Fisher Scientific). The specimens were observed under an Olympus FluoView FV1000 confocal microscope (Olympus Lifescience, Tokyo, Japan), and images were reconstructed in three dimensions using Imaris 6.4.0 (Bitplane, Zurich, Switzerland).

In Vivo Experiments: Grafts from different groups were assembled into 17 mm electrospun poly(ϵ-caprolactone) nerve conduits. Adult male SD rats weighing 230–260 g were anesthetized using 1% entobarbital sodium (40 mg kg^{-1}). The left sciatic nerve was exposed, and a 15 mm nerve defect was created. The grafts from one of the groups were sutured to the nerve defect, and the three surrounding nerves were sutured with nylon sutures (10-0; Ethicon Inc., Raritan, NJ). In the autograft group, a 15 mm transverse nerve segment was sutured under a microscope. For the entire study period, the animals were allowed to obtain food and water in a standard manner to allow them to recover for 12 weeks.

Immunofluorescence Analysis of In Vivo Regenerated Nerves: At 12 weeks postoperatively, the graft midsagittal sections were fixed with 4% w/v polyformaldehyde. The samples were then cut into cross-sections with a thickness of 10 µm using a cryostat sectioning system (CM1950, Leica, Germany). Immunostaining of the sections was performed as previously described. S100 protein antibody (1:200, ab52642; Abcam) and mouse anti-NF160 antibody (1:2000; Cell Signaling Technology, Danvers, MA) were used. The samples were observed under a confocal microscope. The numbers of regenerated axons and myelin sheaths were measured using Image-Pro Plus 6.0 software.

FG Retrograde Tracing: Twelve weeks after surgery, retrograde labeling was performed according to the authors' previous protocol. The transverse spinal cord sections were 25 µm thick, and the DRG longitudinal sections were 10 µm thick. The samples were observed under a Leica DM6000 fluorescence microscope (Leica, Wetzlar, Germany). The numbers of spinal motor neurons and DRG sensory neurons labeled with FG were counted.

Morphological Analysis: At 12 weeks postoperatively, 2 mm nerve segments were harvested 1 mm distal to the graft. The samples were fixed in 3% formaldehyde, post-fixed in 1% osmium tetroxide, and embedded in epoxy resin. The sections were cut into 1.0 µm semi-thin sections and 50 nm ultrathin sections. The semi-thin sections were stained with 1% toluidine blue, and the ultrathin sections were stained with uranyl acetate and lead citrate; both were observed under a transmission electron microscope (H-600; Hitachi Tokyo, Japan). The total number of myelinated axons was calculated from the semi-thin sections. The average diameter, myelin thickness, and axon-to-fiber diameter ratio (*G*-ratio) of the myelinated axons were quantified from the TEM images. The diameters of the myelinated axons and myelinated fibers were measured using Image Pro Plus 6.0 software. At least 200 myelinated fibers were measured in each sample section.

Muscle Weight and Histology Analysis: The animals were deeply anesthetized. The contralateral and ipsilateral soleus muscles were dissected and weighed immediately. The relative wet weight ratio of the muscles was calculated by normalizing the ipsilateral muscle weight to the contralateral weight. Samples from the middle of the soleus muscle were collected, fixed, and stained with Masson's trichrome. The transverse muscle area was observed under a microscope (Olympus Lifescience). Five regions in each part were randomly selected and measured using Image-Pro Plus 6.0 software. At least 200 muscle fibers were measured in each sample section.

Stride Functional Index: Gait analysis was performed to evaluate the recovery of motor function. Briefly, the hind paws of the rats were stained before they were placed on white paper on the track. The stride function index was calculated using the following formula: $109.5(ETS - NTS)/NTS + 13.3(EIT - NIT)/NIT - 38.3(EPL - NPL)/NPL - 8.8$, where PL is the paw length, TS is the toe spread distance between toes one and five, and IT is the toe tip spread distance between toes two and four. All three measurements were obtained from the normal (*N*) and experimental (*E*) sides.

Electrophysiological Evaluation: After gait analysis, electrophysiological evaluation was performed at 4, 8, and 12 weeks. CMAP was recorded from the ipsilateral side using a multi-channel electrophysiological recorder (BL-420N, Techman, China). The CMAP latency was defined as the delay between the stimulus artifact and the first deflection of the

CMAP curve. As the stimulation intensity increased, the CMAP increased continuously, and the CMAP latency was measured at supramaximal stimulation intensities. The distance between the electrodes was then measured, and nerve conduction velocity (NCV) was calculated based on the CMAP recordings. Finally, the peak amplitudes of CMAP, NCV, and CMAP latency were compared between the groups.

Statistical Analysis: All data were expressed as mean ± standard deviation (SD) and presented without further preprocessing. All experiments comprised at least three independent experimental batches or thrice repeated experiments performed under identical conditions ($n \geq 3$). For parametric results, statistical analysis was performed by one-way analysis of variance (ANOVA) with a Tukey–Kramer post hoc test of the variance. In all cases, significance levels (p-values) were indicated with asterisks and specific p-values were provided in each figure legend ($*p < 0.05$, $**p < 0.01$, $***p < 0.001$).

Supporting Information

Supporting Information is available from the Wiley Online Library or from the author.

Acknowledgements

This work was supported by the National Key Research and Development Program of China (SQ2020YFB130100), the CAS Project for Young Scientists in Basic Research (YSBR-041), the National Natural Science Foundation of China (52205319), the Research Equipment Development Program of CAS (YJKYYQ20190045), and the Foundation of State Key Laboratory of Robotics (2022-Z04 and 2023-Z01).

Conflict of Interest

The authors declare no conflict of interest.

Author Contributions

H.W., Y.H., and K.G. contributed equally to this work. Conceptualization: H.W., X.Z., and J.H. Methodology: H.W., Y.H., K.G., B.X., and X.G. Investigation: H.W., Y.H., and K.G. Visualization: H.W., Y.H., and K.G. Supervision: L.L., X.Z., and J.H. Writing—original draft: H.W., Y.H., and K.G. Writing—review and editing: H.W., X.Z., and J.H.

Data Availability Statement

The data that support the findings of this study are available in the supplementary material of this article.

Keywords

collagen, gradient printing, micro-extrusion bioprinting, peripheral nerve graft, structural and chemical guidance

Received: October 12, 2023
Revised: November 14, 2023
Published online: November 30, 2023

[1] S. V. Murphy, P. De Coppi, A. Atala, *Nat. Biomed. Eng.* **2019**, *4*, 370.
[2] X. Liu, X. Wang, L. Zhang, L. Sun, H. Wang, H. Zhao, Z. Zhang, W. Liu, Y. Huang, S. Ji, J. Zhang, K. Li, B. Song, C. Li, H. Zhang, S. Li, S. Wang, X. Zheng, Q. Gu, *Adv. Healthcare Mater.* **2021**, *10*, 2101405.
[3] A. Lee, A. R. Hudson, D. J. Shiwarski, J. W. Tashman, T. J. Hinton, S. Yerneni, J. M. Bliley, P. G. Campbell, A. W. Feinberg, *Science.* **2019**, *365*, 482.
[4] N. E. Fedorovich, J. Alblas, W. E. Hennink, F. C. Öner, W. J. A. Dhert, *Trends Biotechnol.* **2011**, *29*, 601.
[5] C. Frantz, K. M. Stewart, V. M. Weaver, *J. Cell Sci.* **2010**, *123*, 4195.
[6] O. Chaudhuri, J. Cooper-White, P. A. Janmey, D. J. Mooney, V. B. Shenoy, *Nature.* **2020**, *584*, 535.
[7] E. R. Ghomi, N. Nourbakhsh, M. A. Kenari, M. Zare, S. Ramakrishna, *J Biomed Mater Res.* **2021**, *109*, 1986.
[8] K. Lin, D. Zhang, M. H. Macedo, W. Cui, B. Sarmento, G. Shen, *Adv. Funct. Mater.* **2018**, *29*, 1804943.
[9] Y. Fang, C. Wang, Z. Liu, J. Ko, L. Chen, T. Zhang, Z. Xiong, L. Zhang, W. Sun, *Adv. Sci.* **2023**, *10*, 2205744.
[10] B. Kaplan, U. Merdler, A. A. Szklanny, I. Redenski, S. Guo, Z. Bar-Mucha, N. Michael, S. Levenberg, *Biomaterials.* **2020**, *251*, 120062.
[11] J. Zhang, Y. Chen, Y. Huang, W. Wu, X. Deng, H. Liu, R. Li, J. Tao, X. Li, X. Liu, M. Gou, *Adv. Sci.* **2020**, *7*, 2002601.
[12] M. M. Onesto, C. A. Short, S. K. Rempel, T. S. Catlett, T. M. Gomez, *Front Neurosci.* **2021**, *15*, 678454.
[13] J. Seo, W. Youn, J. Y. Choi, H. Cho, H. Choi, C. Lanara, E. Stratakis, I. S. Choi, *Dev. Neurobiol.* **2020**, *80*, 361.
[14] Z. Chen, H. Zhang, C. Fan, Y. Zhuang, W. Yang, Y. Chen, H. Shen, Z. Xiao, Y. Zhao, X. Li, J. Dai, *ACS Nano.* **2022**, *16*, 1986.
[15] L. Huang, J. Gao, H. Wang, B. Xia, Y. Yang, F. Xu, X. Zheng, J. Huang, Z. Luo, *ACS Appl. Mater. Interfaces.* **2020**, *12*, 48380.
[16] E. B. Petcu, R. Midha, E. Mccoll, A. Popa-Wagner, T. V. Chirila, P. D. Dalton, *Biofabrication.* **2018**, *10*, 032001.
[17] X. Li, M. Li, J. Sun, Y. Zhuang, J. Shi, D. Guan, Y. Chen, J. Dai, *Small.* **2016**, *12*, 5009.
[18] H. Wang, X. Liu, Q. Gu, X. Zheng, *Cell Proliferation.* **2023**, *56*, e13453.
[19] K. Liu, L. Yan, R. Li, Z. Song, J. Ding, B. Liu, X. Chen, *Adv. Sci.* **2022**, *9*, 2103875.
[20] D.-L. Chen, P.-F. Yang, Y.-S. Lai, *Microelectron. Reliab.* **2012**, *52*, 541.
[21] N. Saboo, A. Mudgal, *Pet. Sci. Technol.* **2018**, *36*, 1627.
[22] J. Zhang, X. Zhang, C. Wang, F. Li, Z. Qiao, L. Zeng, Z. Wang, H. Liu, J. Ding, H. Yang, *Adv. Healthcare Mater.* **2021**, *10*, 2000604.
[23] A. Schwab, R. Levato, M. D'este, S. Piluso, D. Eglin, J. Malda, *Chem. Rev.* **2020**, *120*, 11028.
[24] H. Wang, K. Guo, L. Zhang, H. Zhu, S. Li, S. Li, F. Gao, X. Liu, Q. Gu, L. Liu, X. Zheng, *Biofabrication.* **2021**, *13*, 035001.
[25] T. H. Qazi, M. R. Blatchley, M. D. Davidson, F. M. Yavitt, M. E. Cooke, K. S. Anseth, J. A. Burdick, *Cell Stem Cell.* **2022**, *29*, 678.
[26] W. J. Rosoff, J. S. Urbach, M. A. Esrick, R. G. Mcallister, L. J. Richards, G. J. Goodhill, *Nat. Neurosci.* **2004**, *7*, 678.
[27] K. Guo, H. Wang, S. Li, H. Zhang, S. Li, H. Zhu, Z. Yang, L. Zhang, P. Chang, X. Zheng, *ACS Appl. Mater. Interfaces.* **2021**, *13*, 7037.
[28] K. Guo, H. Wang, S. Li, P. Chang, C. He, Q. Sun, X. Zheng, *Biofabrication.* **2023**, *15*, 035007.
[29] J. Lou, S. Friedowitz, K. Will, J. Qin, Y. Xia, *Adv. Mater.* **2021**, *33*, 2104460.
[30] A. J. Seymour, A. D. Westerfield, V. C. Cornelius, M. A. Skylar-Scott, S. C. Heilshorn, *Biofabrication.* **2022**, *14*, 022002.
[31] J. S. Miller, K. R. Stevens, M. T. Yang, B. M. Baker, D.-H. T. Nguyen, D. M. Cohen, E. Toro, A. A. Chen, P. A. Galie, X. Yu, R. Chaturvedi, S. N. Bhatia, C. S. Chen, *Nat. Mater.* **2012**, *11*, 768.
[32] L. Zhang, H. Zhang, H. Wang, K. Guo, H. Zhu, S. Li, F. Gao, S. Li, Z. Yang, X. Liu, X. Zheng, *3D Print. Addit. Manuf.* **2023**, *10*, 1046.
[33] A. K. Gaharwar, L. M. Cross, C. W. Peak, K. Gold, J. K. Carrow, A. Brokesh, K. A. Singh, *Adv. Mater.* **2019**, *31*, 1900332.
[34] C. Li, L. Ouyang, J. P. K. Armstrong, M. M. Stevens, *Trends Biotechnol.* **2021**, *39*, 150.
[35] J. M. Lowen, J. K. Leach, *Adv. Funct. Mater.* **2020**, *30*, 1909089.

[36] M. Wang, W. Li, L. S. Mille, T. Ching, Z. Luo, G. Tang, C. E. Garciamendez, A. Lesha, M. Hashimoto, Y. S. Zhang, *Adv. Mater.* **2022**, *34*, 2107038.
[37] C. Bader, D. Kolb, J. C. Weaver, S. Sharma, A. Hosny, J. Costa, N. Oxman, *Sci. Adv.* **2018**, *4*, eaas8652.
[38] P. A. G. S. Giachini, S. S. Gupta, W. Wang, D. Wood, M. Yunusa, E. Baharlou, M. Sitti, A. Menges, *Sci. Adv.* **2020**, *6*, eaay0929.
[39] M. Zeng, Y. Du, Q. Jiang, N. Kempf, C. Wei, M. V. Bimrose, A. N. M. Tanvir, H. Xu, J. Chen, D. J. Kirsch, J. Martin, B. C. Wyatt, T. Hayashi, M. Saeidi-Javash, H. Sakaue, B. Anasori, L. Jin, M. D. Mcmurtrey, Y. Zhang, *Nature.* **2023**, *617*, 292.
[40] D. T. Nguyen, T. D. Yee, N. A. Dudukovic, K. Sasan, A. W. Jaycox, A. M. Golobic, E. B. Duoss, R. Dylla-Spears, *Adv. Mater. Technol.* **2019**, *4*, 1900784.
[41] Y. S. Zhang, G. Haghiashtiani, T. Hübscher, D. J. Kelly, J. M. Lee, M. Lutolf, M. C. Mcalpine, W. Y. Yeong, M. Zenobi-Wong, J. Malda, *Nat Rev Methods Primers.* **2021**, *1*, 75.
[42] A. Reid, J. C. Jackson, J. F. C. Windmill, *Soft Matter.* **2021**, *17*, 1881.
[43] M. A. Skylar-Scott, S. G. M. Uzel, L. L. Nam, J. H. Ahrens, R. L. Truby, S. Damaraju, J. A. Lewis, *Sci. Adv.* **2019**, *5*, eaaw2459.
[44] N. M. Larson, J. Mueller, A. Chortos, Z. S. Davidson, D. R. Clarke, J. A. Lewis, *Nature.* **2023**, *613*, 682.
[45] M. Hajimiri, S. Shahverdi, G. Kamalinia, R. Dinarvand, *J. Biomed. Mater. Res., Part A.* **2015**, *103*, 819.
[46] S. Reed, B. Wu, *Ann. Biomed. Eng.* **2014**, *42*, 1528.
[47] S.-C. Hsieh, C.-M. Tang, W.-T. Huang, L.-L. Hsieh, C.-M. Lu, C.-J. Chang, S.-H. Hsu, *J Biomed Mater Res.* **2011**, *99A*, 576.
[48] Y. Ikegami, H. Ijima, *J. Biosci. Bioeng.* **2020**, *129*, 354.
[49] S. A. Fisher, R. Y. Tam, A. Fokina, M. M. Mahmoodi, M. D. Distefano, M. S. Shoichet, *Biomaterials.* **2018**, *178*, 751.
[50] N. Broguiere, I. Lüchtefeld, L. Trachsel, D. Mazunin, R. Rizzo, J. W. Bode, M. P. Lutolf, M. Zenobi-Wong, *Adv. Mater.* **2020**, *32*, 1908299.